IEEE CSS

Received 7 February 2022; revised 24 April 2022; accepted 22 May 2022. Date of publication 8 June 2022;
date of current version 12 July 2022. The review of this article was arranged by Associate Editor P. Seiler.

Digital Object Identifier 10.1109/OJCSYS.2022.3181111

The Generalized Lyapunov Demodulator: High-Bandwidth, Low-Noise Amplitude and Phase Estimation

MICHAEL R. P. RAGAZZON [1], SAVERIO MESSINEO [2] (Member, IEEE), JAN TOMMY GRAVDAHL [1] (Senior Member, IEEE), DAVID M. HARCOMBE [3], AND MICHAEL G. RUPPERT [3] (Member, IEEE)

[1]Department of Engineering Cybernetics, Norwegian University of Science and Technology, 7034 Trondheim, Norway
[2]Embedded AI, Silicon Austria Labs, 4040 Linz, Austria
[3]School of Engineering, University of Newcastle, Callaghan, NSW 2308, Australia

CORRESPONDING AUTHOR: MICHAEL R. P. RAGAZZON (e-mail: michael@ragazzon.no)

This work was supported in part by H2020 European Research Council under Grant 101017697-CRÈME and in part by Norges Forskningsråd under Grants 223254 and 304667.

ABSTRACT Effective demodulation of amplitude and phase is a requirement in a wide array of applications. Recent efforts have increased the demodulation performance, in particular, the Lyapunov demodulator allows bandwidths up to the carrier frequency of the signal. However, being inherently restricted to first-order filtering of the input signal, it is highly sensitive to frequency components outside its passband region. This makes it unsuitable for certain applications such as multifrequency atomic force microscopy (AFM). In this article, the structure of the Lyapunov demodulator is transformed to an equivalent form and generalized by exploiting the internal model principle. The resulting generalized Lyapunov demodulator structure allows for arbitrary filtering order and is easy to implement, requiring only a bandpass filter, a single integrator, and two nonlinear transformations. The generalized Lyapunov demodulator is implemented experimentally on a field-programmable gate array (FPGA). Then it is used for imaging in an AFM and benchmarked against the standard Lyapunov demodulator and the widely used lock-in amplifier. The lock-in amplifier achieves great noise attenuation capabilities and off-mode rejection at low bandwidths, whereas the standard Lyapunov demodulator is shown to be effective at high bandwidths. We demonstrate that the proposed demodulator combines the best from the two state-of-the-art demodulators, demonstrating high bandwidths, large off-mode rejection, and excellent noise attenuation simultaneously.

INDEX TERMS Amplitude estimation, atomic force microscopy, demodulators, feedback, field programmable gate arrays, filters, internal model principle, modeling, optimization, phase estimation.

I. INTRODUCTION

Demodulation is an indispensable technique in a wide array of applications [1]. It can be used in combination with a modulation step to enable the transmission of a signal over a physical medium, or to enhance the signal-to-noise ratio by evading low-frequency noise sources [2]–[5]. Alternatively, demodulation can be used to extract signals from inherently modulated sources, such as an oscillating cantilever in dynamic mode atomic force microscopy (AFM) [6], [7].

In dynamic mode AFM, a demodulator is located within the vertical feedback loop controlling the distance between the cantilever and the sample being imaged. Thus, the bandwidth of the demodulator directly imposes a limitation on the achievable imaging speed [8]. Simultaneously, the demodulator is of vital importance to ensure attenuation of noise and possibly undesired harmonics and other distortions commonly present in the signal. The lock-in amplifier is a commonly used synchronous demodulator in applications where effective noise attenuation is desired, in particular when combined with a higher order lowpass filter to achieve strong filtering behavior [3], [4], [7]. However, the lock-in amplifier inherently suffers from mixing products that generate harmonics at twice

the carrier frequency, $2f_c$, which unavoidably appear at high demodulation bandwidths [8], [9].

Other demodulators have been proposed in AFM for overcoming this limitation, including the high-bandwidth lock-in amplifier [10], the coherent demodulator [11], [12], the Kalman filter-based demodulator [13], and the Lyapunov demodulator [14]. However, these demodulators perform worse in terms of noise suppression, especially at lower bandwidths, compared to the lock-in amplifier [8].

The Lyapunov demodulator in particular has been shown to allow for some of the highest bandwidths, up to the carrier frequency of the signal, completely avoiding the limitations due to the lock-in amplifier's $2f_c$ mixing products [14]. Simultaneously, it is simple to implement as it requires only a low number of arithmetic operations, has a low computational complexity, and is relaxed in terms of timing requirements [8]. On the other hand, the Lyapunov demodulator acts like a first-order filter in terms of noise filtering, thus, the resulting demodulated signal is prone to noise and other distortions.

The Lyapunov demodulator has been extended to multifrequency AFM, thus eliminating distortions from the frequencies or harmonics that are modeled as part of the demodulator [15], [16]. However, there is still a desire to increase the filtering order to attenuate noise and unmodeled frequency components outside the passband region of the demodulator, hereby denoted as off-mode rejection [8].

Extensions to the standard Lyapunov demodulator, involving linear time-invariant (LTI) representations of the demodulator, have been explored to allow for higher order filtering characteristics [17], [18]. However, these approaches require a controller parameterization or linearization which ultimately constrain the design degree of freedom of the resulting demodulators.

In the preliminary results presented in [19], the authors introduced a generalization of the Lyapunov demodulator where the need for controller parameterization or linearization is circumvented. Instead, the filter is designed directly using standard bandpass filter design techniques without modifications and analyzed using standard tools for LTI systems. By exploiting the internal model principle [20]–[23], conditions are found under which perfect tracking of amplitude and phase is guaranteed. This resulted in a flexible demodulator achieving both high filter order and high tracking bandwidth simultaneously, within a framework which allows for both easy design and implementation.

This article includes the main results of, and extends the preliminary results of [19] where the generalized Lyapunov demodulator was first proposed. In particular, the following additional results are new to this article: *(a)* additional performance metrics including error bandwidth and noise attenuation, *(b)* the integration of optimized bandpass filters using a multi-objective solver, *(c)* a derived expression for the gain as a function of bandwidth for the standard and higher order Lyapunov demodulators, *(d)* comparisons to the lock-in amplifier, and *(e)* experimental results.

For the experiments, we chose to implement the generalized Lyapunov demodulator on a field-programmable gate array (FPGA) to enable high-speed demodulation [16], [24]. The proposed demodulator has been benchmarked at a variety of bandwidth settings using different bandpass filters. In addition, the standard Lyapunov filter and a lock-in amplifier have also been implemented on the FPGA and compared to the proposed demodulator. Finally, the generalized Lyapunov demodulator has been employed and used for imaging in an AFM to demonstrate the feasibility of the proposed demodulator.

The article proceeds as follows. In Section II the standard Lyapunov demodulator is introduced, and several key demodulation performance metrics are presented. Then, the generalized Lyapunov demodulator is developed in Section III, whose pre-filtering step enables an additional design degree of freedom. In Section IV design criteria for the shape of the filter are discussed and several filters are proposed. Then, the experimental setup is introduced in Section V and experimental results are presented in Section VI. Finally, conclusions are given in Section VII.

II. LYAPUNOV DEMODULATOR

A. PROBLEM FORMULATION

Consider a sinusoidal signal $r(t)$ with angular carrier frequency $\omega_c = 2\pi f_c$, and varying amplitude $a^*(t)$ and phase $\varphi^*(t)$ of the following form

$$r(t) = a^*(t)\sin\left(\omega_c t + \varphi^*(t)\right). \tag{1}$$

In the demodulation problem considered in this article, the carrier frequency is considered known while the amplitude and phase signals are to be estimated. In the remainder of the article, signals will be typed without their explicit dependency on time for ease of notation, and the formula $\omega_k = 2\pi f_k$ will hold generally for any given k.

The formula (1) can be rewritten using the in-phase and quadrature components of the sinusoid,

$$\begin{aligned} r &= [\cos(\omega_c t),\ \sin(\omega_c t)]\begin{bmatrix} a^*\sin\varphi^* \\ a^*\cos\varphi^* \end{bmatrix}, \\ &= \boldsymbol{c}^T\boldsymbol{x}^*, \end{aligned} \tag{2}$$

where

$$\boldsymbol{c} = [\cos(\omega_c t),\ \sin(\omega_c t)]^T, \tag{3}$$

$$\boldsymbol{x}^* = [x_1^*,\ x_2^*]^T = [a^*\sin\varphi^*,\ a^*\cos\varphi^*]^T. \tag{4}$$

The amplitude and phase can then be recovered using a standard Cartesian to polar coordinate transformation,

$$a^* = \sqrt{x_1^{*2} + x_2^{*2}}, \quad \varphi^* = \operatorname{atan2}(x_1^*,\ x_2^*), \tag{5}$$

where $\operatorname{atan2}(\cdot,\cdot)$ is the four-quadrant inverse tangent function.

B. STANDARD LYAPUNOV DEMODULATOR

The Lyapunov method can be used to estimate parameters in linear parametric models such as in (2), and guarantees

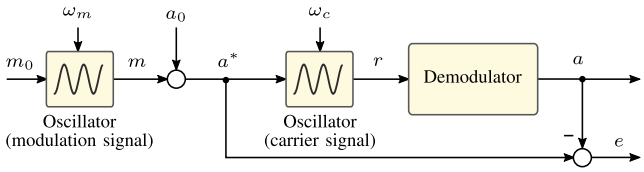

FIGURE 1. Block diagram for measurement of the demodulator metrics. Here, the amplitude estimate a is considered, however, the setup could equivalently be used for the phase estimate φ.

exponential convergence to the real parameters under certain conditions [25]. The Lyapunov demodulator in particular satisfies these conditions, and can be used to effectively estimate the amplitude and phase of a measured signal [14].

The Lyapunov demodulator can be written in the linear time-varying form

$$\dot{\boldsymbol{x}} = \gamma \boldsymbol{c} \varepsilon,$$
$$y = \boldsymbol{c}^T \boldsymbol{x}, \tag{6}$$

where $\varepsilon = r - y$, the constant gain parameter $\gamma > 0$ determines the demodulation bandwidth, the state vector $\boldsymbol{x} = [x_1, x_2]^T$, and the signal vector $\boldsymbol{c}$ is given by (3).

Since $\boldsymbol{x}$ represents the estimated in-phase and quadrature components of the sinusoid, the estimated amplitude a and phase φ can be recovered as in (5) but applied to the estimator state vector $\boldsymbol{x}$,

$$a = \sqrt{x_1^2 + x_2^2}, \quad \varphi = \operatorname{atan2}(x_1, x_2). \tag{7}$$

Next, simulations of the standard Lyapunov demodulator are performed to demonstrate some of its characteristics and limitations, while exploring important metrics used throughout the article to evaluate the performance of the presented demodulators.

C. SIMULATION: TRACKING RESPONSE

The tracking ($\mathcal{T}$) frequency response for demodulators is determined by applying a sinusoidal reference amplitude

$$a^* = a_0 + m_0 \cos(\omega_m t) \tag{8}$$

for some constants a_0, m_0 at incrementally increasing values of ω_m, as illustrated in Fig. 1 where $m = m_0 \cos(\omega_m t)$ is the modulation signal. For each value of ω_m the amplitude estimate output a is measured. Then, the discrete Fourier transform (DFT) at that frequency is computed to isolate the estimate of the modulation magnitude m_0, using a second-order Goertzel algorithm [26].

Using the described approach, the tracking response of the Lyapunov demodulator with $f_c = 50\,\text{kHz}$ at increasing bandwidth settings γ is plotted in Fig. 2(a). The first-order filtering capabilities of the standard Lyapunov filter is seen by the approximate $-20\,\text{dB/dec}$ magnitude roll-off above its cutoff frequency. It is desirable to increase the magnitude roll-off to reduce the impact of measurement noise and disturbances, which is only possible by increasing the filter order of the demodulator [27].

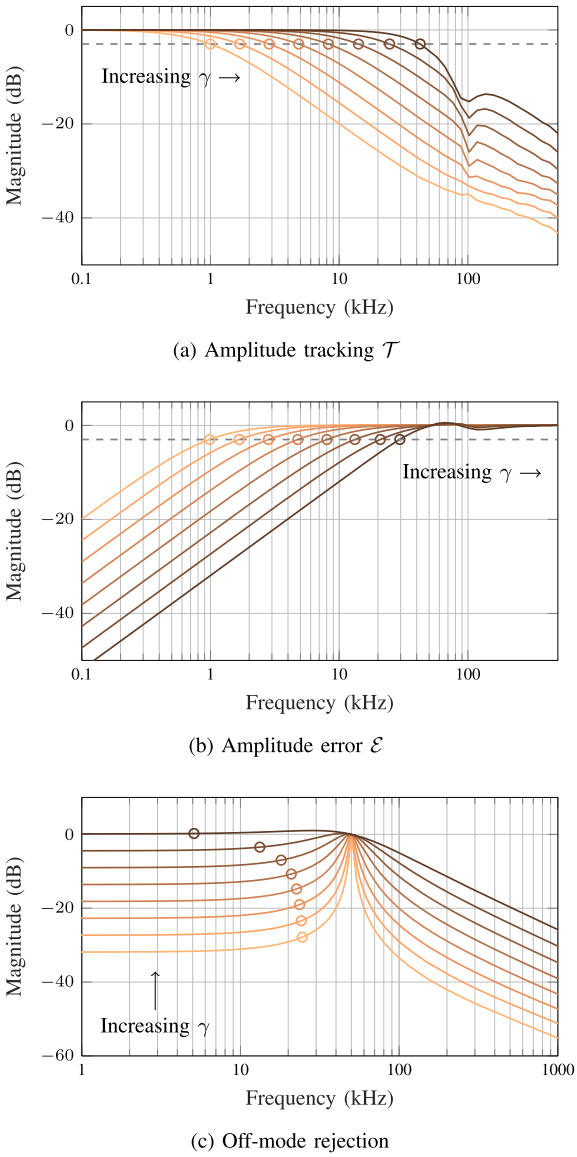

(a) Amplitude tracking $\mathcal{T}$

(b) Amplitude error $\mathcal{E}$

(c) Off-mode rejection

FIGURE 2. Simulations of the standard Lyapunov demodulator at increasing bandwidth gain γ. Circles mark the quantitative measurement of the metric at that gain setting, while the dashed lines mark the -3 dB magnitude.

D. SIMULATION: ERROR RESPONSE

The error ($\mathcal{E}$) frequency response is determined as for the tracking bandwidth, except that the magnitude is now measured in terms of the error signal $e = a^* - a$ instead of the amplitude estimate output. This can be considered a more accurate metric for the practically usable bandwidth [27]. The error frequency response of the standard Lyapunov filter is shown in Fig. 2(b).

E. SIMULATION: OFF-MODE REJECTION

A desirable property for demodulators is the attenuation of frequency components outside the passband region. To determine this property, the demodulator is fixed at a given setting for the bandwidth and the carrier frequency. Then, the input

signal r is swept using a sinusoid of increasing frequency, that is, by setting $a^* = 1$ and sweeping ω_c in Fig. 1. At each frequency step, the magnitude of the amplitude estimate from the demodulator at steady-state is recorded, thereby measuring the amplitude estimate response resulting from a carrier signal of increasing frequency.

The described procedure is repeated at increasing bandwidth settings for the Lyapunov demodulator, and the results are plotted in Fig. 2(c). This shows the attenuation of frequency components outside the modeled carrier frequency and is therefore termed *off-mode rejection*. In particular, the Lyapunov demodulator is characterized by a low off-mode rejection which flattens out at lower frequencies. Higher off-mode rejection is achieved by decreasing the tracking bandwidth or increasing the filter order [8]. This demonstrates the desire to increase the filter order of the Lyapunov demodulator.

F. QUANTITATIVE MEASUREMENTS

The introduced metrics show important performance characteristic of a given demodulator in the frequency domain. For each of the three metrics, it is also desirable to retrieve a single quantitative value for comparison purposes. The quantitative measurements are marked for each of the simulation results shown in Fig. 2.

1) TRACKING BANDWIDTH

The tracking bandwidth is used as a quantitative measurement for the tracking response, defined as the frequency at which the magnitude crosses -3 dB from above.

2) ERROR BANDWIDTH

The error bandwidth is used as a quantitative measurement for the error response, defined as the frequency at which the magnitude crosses -3 dB from below.

3) OFF-MODE REJECTION

A quantitative measurement of the off-mode rejection is defined as the reciprocal of the measured magnitude at the frequency f_{omr} given by

$$f_{omr} = \tfrac{1}{2}(f_c - f_b), \tag{9}$$

where f_b is the tracking bandwidth of the demodulator. This measurement captures the noise suppression performance at the frequency halfway between steady-state and the lower cutoff frequency of the passband region, where significant attenuation is normally desired and expected. The defined frequency ensures that the metric is effective at any demodulator bandwidth setting less than the carrier frequency.

III. GENERALIZED LYAPUNOV DEMODULATOR

In this section, the generalized Lyapunov demodulator is developed, being the main contribution of this article. The standard Lyapunov demodulator is limited by its first-order filtering capabilities. Ideally, we would like to increase the off-mode rejection of the demodulator without decreasing the bandwidth, which is only possible with increased filtering order. In the following, the standard Lyapunov demodulator is recast and generalized to allow for filtering of arbitrary order and flexible filter shaping.

A. INTERNAL MODEL REPRESENTATION

The standard Lyapunov demodulator is first recast to incorporate an *internal model* of the sinusoidal signal r [21]. Consider the signal r in (1) with a slowly varying amplitude and phase. This sinusoid can equivalently be represented by the output of the following system

$$\begin{aligned} \dot{\boldsymbol{w}} &= \mathbf{S}\boldsymbol{w}, \\ \boldsymbol{w}(0) &= \boldsymbol{w}_0, \\ r &= \boldsymbol{\Gamma}^T \boldsymbol{w}, \end{aligned} \tag{10}$$

for some $\boldsymbol{w}_0$ with $\boldsymbol{\Gamma} = [1, 0]^T$ and

$$\mathbf{S} = \begin{bmatrix} 0 & \omega_c \\ -\omega_c & 0 \end{bmatrix}. \tag{11}$$

With the definition of the rotation matrix

$$\mathbf{R}(\omega_c t) = \begin{bmatrix} \cos\omega_c t & \sin\omega_c t \\ -\sin\omega_c t & \cos\omega_c t \end{bmatrix}, \tag{12}$$

(11)–(12) imply that

$$e^{\mathbf{S}t} = \mathbf{R}(\omega_c t). \tag{13}$$

By the change of coordinates $\boldsymbol{v} = [v_1, v_2]^T = e^{\mathbf{S}t}\boldsymbol{x}$ applied to (6), the following system is retrieved,

$$\begin{aligned} \dot{\boldsymbol{v}} &= \mathbf{S}\boldsymbol{v} + \gamma\boldsymbol{\Gamma}\varepsilon, \\ y &= \boldsymbol{\Gamma}^T \boldsymbol{v}. \end{aligned} \tag{14}$$

System (14) is a linear time-invariant formulation of the standard Lyapunov demodulator, said to incorporate an internal model of the sinusoid r.

B. GENERALIZED LYAPUNOV DEMODULATOR

In order to allow for arbitrary higher order filtering techniques, we propose to extend the system (14) by replacing the pure gain γ by a filter

$$\begin{aligned} \dot{\boldsymbol{\eta}} &= \mathbf{A}\boldsymbol{\eta} + \mathbf{B}\varepsilon, \\ u &= \mathbf{C}\boldsymbol{\eta}, \end{aligned} \tag{15}$$

where $\mathbf{A} \in \mathbb{R}^{m\times m}$, $\mathbf{B} \in \mathbb{R}^{m\times 1}$, $\mathbf{C} \in \mathbb{R}^{1\times m}$ and m are design parameters, and $\mathbf{A}$ is Hurwitz.

Then, from (14),(15), the overall extended version of the Lyapunov demodulator can be written as follows

$$\begin{aligned} \dot{\boldsymbol{\eta}} &= \mathbf{A}\boldsymbol{\eta} + \mathbf{B}\varepsilon, \\ \dot{\boldsymbol{v}} &= \mathbf{S}\boldsymbol{v} + \boldsymbol{\Gamma}\mathbf{C}\boldsymbol{\eta}, \\ y &= \boldsymbol{\Gamma}^T \boldsymbol{v}. \end{aligned} \tag{16}$$

The generalized form of the Lyapunov demodulator (16) is a linear time-invariant system, thus ensuring the applicability of

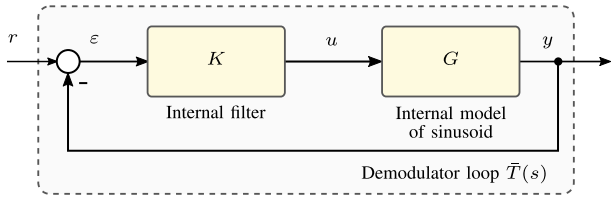

FIGURE 3. Block diagram of the demodulator loop.

common control design techniques, in contrast to the standard Lyapunov demodulator (6).

A block diagram of the closed-loop response from r to y, termed the *demodulator loop* $\bar{T}(s)$, is shown in Fig. 3. Here, $G(s)$ represents the transfer function of the system (14) with $\gamma = 1$, such that

$$G(s) = \mathbf{\Gamma}^T(s\mathbf{I} - \mathbf{S})^{-1}\mathbf{\Gamma} = \frac{s}{s^2 + \omega_c^2}, \tag{17}$$

which is corroborated by the results presented in [17]. The gain γ is replaced by the transfer function $K(s)$ representing the system (15). That is,

$$K(s) = \mathbf{C}(s\mathbf{I} - \mathbf{A})^{-1}\mathbf{B}. \tag{18}$$

Then, any standard control design technique can be used to find a suitable transfer $K(s)$ for some desired response of the demodulator loop, under the constraint of closed-loop stability [27], [28]. This can be done in the frequency-domain by shaping the loop $L(s) = G(s)K(s)$ or the closed-loop $\bar{T}(s)$, or we could work in the time-domain by selecting $\mathbf{A}, \mathbf{B}, \mathbf{C}$ in (15). This way, the filter order of the demodulator can be increased, and its filter shaped so that the demodulator satisfies some given performance constraints.

Remark 1: The sinusoidal input signal is treated as a reference signal to be tracked. By virtue of the internal model principle, perfect tracking in the stationary sense is achieved for any stabilizing filter $K(s)$.

Remark 2: The tracking bandwidth $\mathcal{T}$ frequency response introduced in Section II is not comparable to the demodulator loop $\bar{T}(s)$. The former measures the input-output response of any demodulator, while the demodulator loop is internal to the generalized Lyapunov demodulator.

C. COLLAPSING THE DEMODULATOR LOOP

The generalized demodulator structure (16) allows the inclusion of a filter, thereby extending the filtering capabilities of the Lyapunov demodulator. Let $T(s)$ denote the *desired shape* of the demodulator loop. Now it is possible to approximate the desired shape such that $\bar{T}(s) \approx T(s)$ by selecting $K(s)$ while keeping $G(s)$ fixed, analogous to finding a controller in control system design. However, it can be challenging to find a suitable $K(s)$. Moreover, only a limited class of controllers is admissible for a given overall desired closed-loop demodulator response, in particular under the constraint that the controller must be realizable, causal, and lead to an internally stable feedback system [17], [27].

Instead, we propose a direct design approach where the demodulator loop is collapsed, and the desired shape $T(s)$ is employed directly as a filter. This is made possible by exploiting the fact that there are no uncertainties in the demodulator loop $\bar{T}(s)$, every component of the demodulator loop is perfectly known.

In this proposed direct design approach, there is no need to decompose the filter into elements of the feedback loop shown in Fig. 3. The direct use of $T(s)$ allows a more flexible approach and a wider range of admissible filter shapes. As long as the conditions

$$|T(j\omega_c)| = 1, \quad \angle T(j\omega_c) = 0^\circ, \tag{19}$$

are satisfied, the perfect tracking condition still applies. The conditions (19) ensure that the sensitivity function [27] evaluated at the carrier frequency satisfies $S(j\omega_c) = 0$ which results in a stationary tracking error of zero. Alternatively, the perfect tracking condition can be relaxed to allow for an even wider range of permissible filters.

D. COLLAPSED MODEL STATES

In the collapsed system, only the output of $T(s)$ is available which is insufficient for resolving the amplitude and phase estimates. However, this can be resolved by considering the internal model described by (16). Here, we have $\dot{v}_2 = -\omega_c v_1$, thus, an equivalent transfer function for the second state is obtained by

$$T^\perp(s) = -\tfrac{\omega_c}{s} T(s). \tag{20}$$

As in the internal model, this ensures a 90° phase difference between the two states. Thus, once the closed-loop filter $T(s)$ is designed, the second state is retrieved by (20). Then, the output of $T(s), T^\perp(s)$ can be used as v_1, v_2 respectively to retrieve the amplitude and phase as described in the following.

E. RECOVERY OF AMPLITUDE AND PHASE

In order to recover the amplitude and phase, the state variables $\boldsymbol{v}$ in the generalized Lyapunov demodulator (16) must be transformed back to the $\boldsymbol{x}$ coordinates, that is

$$\boldsymbol{x} = \left(e^{\mathbf{S}t}\right)^{-1} \boldsymbol{v}. \tag{21}$$

However, note that $e^{\mathbf{S}t} = \mathbf{R}(\omega_c t)$ is a rotation matrix in the group SO(2) with angle $\omega_c t$ [29]. This allows us to exploit the property $\mathbf{R}(\omega_c t)^{-1} = \mathbf{R}(-\omega_c t)$ such that

$$\boldsymbol{x} = \mathbf{R}(-\omega_c t)\boldsymbol{v}, \tag{22}$$

which increases numerical accuracy and lessens the computational requirements compared to a numerical matrix inverse operation. Now the estimated amplitude and phase can be recovered using (7). With this, the generalized Lyapunov demodulator is complete. The block diagram of the demodulator is shown in Fig. 4.

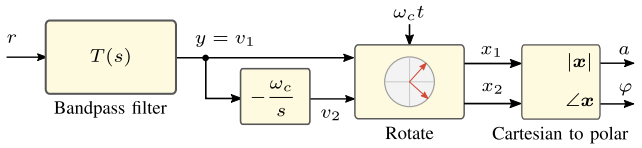

FIGURE 4. Block diagram of the proposed generalized Lyapunov demodulator.

Remark 3: The amplitude is unchanged through the rotation (22), and the angle can also be applied arithmetically after resolving the angle of $\boldsymbol{v}$. Thus, it is also possible to recover the estimates from $\boldsymbol{v}$ directly,

$$a = \sqrt{v_1^2 + v_2^2}, \tag{23}$$

$$\varphi = ((\text{atan2}\,(v_1, v_2) - \omega_c t + \pi) \mod 2\pi) - \pi, \tag{24}$$

where the modulus operator and π-terms ensure $\varphi \in [-\pi, \pi)$.

Remark 4: The evaluation of (24) may be numerically unstable as $t \to \infty$ due to the term $\omega_c t$. This can have practical concerns, especially on platforms with low bit accuracy. Instead, some platforms have dedicated rotation operations ensuring numerical stability, which could be used to find $\boldsymbol{x}$ from $\boldsymbol{v}$ as in (22), and then the amplitude and phase can be recovered using (7). Alternatively, note that the $\mathbf{R}$ matrix uses the sine and cosine carriers already available in $\boldsymbol{c}$. Thus, when the signals of $\boldsymbol{c}$ are available, they can be redirected to build the $\mathbf{R}$ matrix which can then be used to find $\boldsymbol{x}$ in (22).

IV. FILTER DESIGN

The key improvement of the generalized Lyapunov demodulator is the ability to increase the filtering order and shape the filtering behavior as desired. The main design degree of freedom is the choice of the filter $T(s)$ shown in Fig. 4. In this section, the design criteria for $T(s)$ are discussed, and several specific filters are proposed for implementation in the generalized Lyapunov demodulator.

A. FILTER DESIGN CONSIDERATIONS

In the following, the key design criteria for the filter $T(s)$ are examined.

1) SHAPE AND BANDWIDTH

The filter $T(s)$ should be designed as a bandpass filter with center frequency near ω_c and a passband bandwidth about twice the desired tracking bandwidth [1]. This is evident by considering an input signal with sinusoidally varying amplitude $a^* = a_0 + m_0 \cos \omega_m t$ for some constants $\omega_m, a_0 > 0$ and $m_0 < a_0$. Then we have

$$\begin{aligned} r &= a^* \sin \omega_c t \\ &= a_0 \sin \omega_c t + \tfrac{1}{2} m_0 \sin\left[(\omega_c - \omega_m)t\right] \\ &\quad + \tfrac{1}{2} m_0 \sin\left[(\omega_c + \omega_m)t\right]. \end{aligned} \tag{25}$$

Thus, in the frequency domain, the modulation products are moving away from the carrier frequency with increasing ω_m,

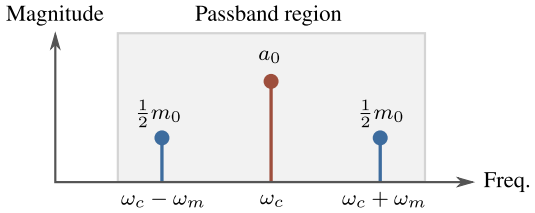

FIGURE 5. The modulation products of a sinusoidal amplitude signal. In order to track a modulated signal of ω_m frequency, the demodulator loop must have a passband region covering $\omega_c \pm \omega_m$.

as shown in Fig. 5. Therefore, the amplitude and phase tracking bandwidth ω_b is about half the passband bandwidth in $T(s)$. However, in cases where the bandpass filter is not exactly symmetric around ω_c, the resulting tracking bandwidth may not correspond to exactly half the passband bandwidth.

2) RELATIVE ORDER

The relative order (relative degree) of a filter is directly related to the magnitude roll-off outside the bandwidth of the signal. This is a prime determining factor for off-mode rejection, a major concern in applications such as multifrequency AFM [9], [30], [31]. In these cases, there are multiple carrier signals. Then, multiple demodulators can be added together in parallel by shaping each $T(s)$ such that they do not overlap for the given carrier frequencies. Then, the steeper roll-off of higher relative order filters allows for increased bandwidth without overlap. Additionally, higher order filtering ensures noise located outside the passband region is effectively attenuated.

3) PHASE DELAY

The transient performance is partly determined by the phase delay. In general, a lower order filter will have a smaller phase delay and improved transient performance. Thus, there is a trade-off between filter order and performance. However, distinct filters of the same order will achieve different steepness of the phase within the passband region, which should be considered during the design of the filter $T(s)$. A minimum-phase filter is desirable.

4) GROUP DELAY

The group delay of a filter $T(s)$, being the derivative of phase with respect to frequency, should ideally be near-constant inside the passband region [2]. A non-constant group delay will make the emergence of sidebands such as in Fig. 5 appear with different time-delays, and can thus be destructive to tracking in the transient regime.

5) AMPLITUDE AND PHASE OFFSETS

If the designed filter $T(s)$ does not satisfy unity magnitude and zero-phase at ω_c as in (19), then the resulting amplitude and phase estimates change correspondingly in the stationary

TABLE 1 Higher Order Lyapunov Filters.

k	$T_k(s)$	$\gamma_k(\omega_b)$
1	$\frac{\gamma_1 s}{s^2+\gamma_1 s+\omega_c^2}$	$\gamma_1 = 2\omega_b$
2	$\frac{\gamma_2^2 s^2}{(s^2+\gamma_2 s+\omega_c^2)^2}$	$\gamma_2 = \frac{2\omega_b}{\sqrt{2^{1/2}-1}}$
3	$\frac{\gamma_3^3 s^3}{(s^2+\gamma_3 s+\omega_c^2)^3}$	$\gamma_3 = \frac{2\omega_b}{\sqrt{2^{1/3}-1}}$
4	$\frac{\gamma_4^4 s^4}{(s^2+\gamma_4 s+\omega_c^2)^4}$	$\gamma_4 = \frac{2\omega_b}{\sqrt{2^{1/4}-1}}$

case. The corrected estimates a_c, φ_c can be obtained from

$$a_c = \frac{a}{|T(j\omega_c)|}, \quad \varphi_c = \varphi - \angle T(j\omega_c). \tag{26}$$

In the remainder of this section, several specific filter implementations are proposed utilizing these design criteria.

B. HIGHER ORDER LYAPUNOV FILTER

The first approach considers a filter design based on the standard Lyapunov demodulator. In order to achieve a better response in terms of off-mode rejection, higher order versions of the Lyapunov demodulator are designed. The closed-loop response $T(s) = G(s)K(s)/(1 + G(s)K(s))$ of the standard Lyapunov demodulator where $K(s) = \gamma$ and using $G(s)$ from (17), gives the transfer function [17]

$$T_1(s) = \frac{\gamma s}{s^2 + \gamma s + \omega_c^2}. \tag{27}$$

The higher order Lyapunov demodulators are then formulated as

$$T_k(s) = T_1(s)^k \tag{28}$$

where k represents the relative order of the filter. The Lyapunov filters $T_k(s)$ can be directly integrated into the generalized Lyapunov demodulator as in Fig. 4.

The tuning parameter γ_k expressed as a function of the desired bandwidth ω_b for the kth relative order Lyapunov filter, is given by

$$\gamma_k = \frac{2\omega_b}{\sqrt{2^{1/k}-1}}, \tag{29}$$

as shown in Appendix A. The Lyapunov filters $T_k(s)$ are listed for relative orders 1–4 along with the gain γ_k as an expression of the desired tracking bandwidth ω_b in Table 1. In the remainder of this article, `Lyap1` denotes the standard Lyapunov demodulator whereas `Lyap3` denotes the higher order Lyapunov demodulator with relative order 3.

C. STANDARD BANDPASS FILTERS

Standard LTI filters can also be used in the generalized Lyapunov demodulator, such as the Butterworth filter, Bessel filter, and Chebyshev type-I filter [17], [19]. Such filters have distinct characteristics in terms of magnitude roll-off, phase response, and group delay [26], [32]. In particular, the Butterworth filter, hereby `Butter`, will be employed in this article. This filter features a relatively steep magnitude roll-off, which in turn should make it perform well in terms of off-mode rejection. Standard filters are commonly given as lowpass prototype filters, in order to achieve the desired bandpass filter shape the prototype must be converted, as detailed in the next section.

D. BANDPASS TRANSFORMATION AND PERFECT TRACKING

The conversion from a lowpass prototype filter to bandpass form is generally needed to employ standard filters. Once a lowpass prototype filter is acquired, the prototype is then converted to bandpass form using an s-domain transformation [32]. However, at high tracking bandwidths, as the carrier frequency of the signal is approached, subtly different conversion approaches result in different performance trade-offs which will be detailed in the following.

Consider $H(s)$ to be a lowpass prototype filter with unity angular cutoff frequency and where $H(0) = 1$. Then, the mapping [32]

$$s \to \frac{1}{2\omega_b}\left(s + \frac{\omega_0^2}{s}\right) \tag{30}$$

applied to $H(s)$ gives a bandpass filter $H_{bp}(s)$, where ω_0 is the resonance frequency and ω_b is the desired demodulator tracking bandwidth, equivalent to half the bandwidth of the resulting bandpass filter. For lowpass filters of order n, the resulting bandpass filters are order $2n$ and relative order n. Let $\omega_0 = \omega_c$, then it can be seen that $H_{bp}(j\omega_c) = H(0) = 1$. Thus, this transformation ensures that the perfect tracking conditions (19) hold.

Ideally, the corner frequencies of the bandpass filter are placed at $\omega_{1,2} = \omega_c \mp \omega_b$ so that the passband region is symmetric around the carrier frequency in accordance with Fig. 5. However, it can be shown that the corner frequencies are given by [32]

$$\omega_{1,2} = \sqrt{\omega_0^2 + \omega_b^2} \mp \omega_b, \tag{31}$$

which is incompatible with the desired placement. Thus, one is forced to choose between

i) $\omega_0 = \omega_c$ for perfect tracking conditions, or
ii) $\omega_0 = \sqrt{\omega_c^2 - \omega_b^2}$ for a symmetric passband region.

At low bandwidths $\omega_b \ll \omega_c$ the difference between these two cases is negligible since $\omega_0 \approx \omega_c$ also for the latter case.

The resulting bandpass filter shapes using each of these approaches on the Butterworth filter is shown in Fig. 6. The perfect tracking approach (i) always results in 0 dB magnitude and 0 deg phase at ω_c, regardless of the shape of the prototype filter, however the passband region is biased towards higher frequencies. Due to the non-symmetry of this approach, the desired bandwidth ω_b does not correspond exactly to the

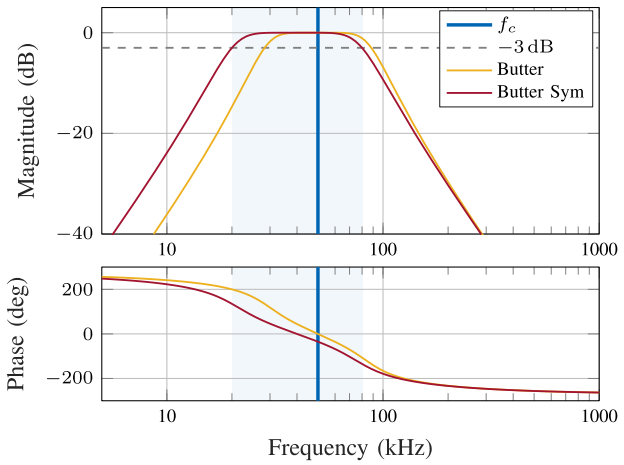

FIGURE 6. Butterworth bandpass filters, using a perfect tracking approach (`Butter`) versus a symmetric shape around f_c (`Butter Sym`). The shaded blue area shows the symmetric passband region.

tracking bandwidth of the resulting demodulator. To compensate, the used value of ω_b must be increased to achieve the desired bandwidth. This has been done in the figure so that the two approaches have matching tracking bandwidths.

On the other hand, the symmetric passband region approach (ii) has phase and magnitude offsets at ω_c. Thus, it needs corrections of the estimated amplitude and phase using (26) to compensate for the violation of the perfect tracking conditions. Specifically, for the Butterworth filter the magnitude offset is close to imperceptible, but other filter prototypes can give significant offsets in magnitude as well as phase.

Generally, the perfect tracking approach (i) performs better in terms of error bandwidth, and is slightly easier to implement since estimation corrections are not necessary. On the other hand, the symmetric approach (ii) behaves better in terms of off-mode rejection since there is no bias towards higher frequencies. In the remainder of this article, we choose to implement the `Butter` filter using the perfect tracking approach.

E. MULTI-OBJECTIVE OPTIMIZATION FILTER

Some applications require large off-mode rejection whereas other desire a quick step response and small tracking errors. However, these objectives are conflicting; by optimizing for only one objective the other can suffer greatly. Instead, in this section we propose to design filters as a multi-objective optimization problem. This way, it is possible to optimize for these two objectives simultaneously, and then choose a particular solution from the set of solutions which provides the best trade-off to suit any given application. This approach has been used in applications ranging from airfoil shape optimization [33], task assignment for human-robot teams [34], to locomotion efficiency in snake robots [35].

The bandpass filter to be optimized is structured as follows,

$$T_P(s;\boldsymbol{\theta}) = g\prod_{k=1}^{n}\frac{s\omega_k}{s^2+2\zeta_k\omega_k+\omega_k^2}, \tag{32}$$

where n is the relative order of the filter, ω_k, ζ_k for $k \in \{1, 2, \ldots, n\}$ are the optimization variables to be decided, $\boldsymbol{\theta} = \{\omega_1, \ldots, \omega_n, \zeta_1, \ldots, \zeta_n\}$, and the gain $g = g(\boldsymbol{\theta})$ is determined such that $|T_P(j\omega_c;\boldsymbol{\theta})| = 1$.

Remark 5: The structure (32) is sufficiently general to encompass a wide selection of bandpass filters, including the higher order Lyapunov and Butterworth filters.

The optimization problem to be solved is specified by

$$\begin{aligned}\min_{\boldsymbol{\theta}} J &= [J_{\mathrm{o}}(\boldsymbol{\theta}),\ J_{\mathrm{r}}(\boldsymbol{\theta})]\\ \text{s.t.}\quad &\boldsymbol{\theta}_l \le \boldsymbol{\theta} \le \boldsymbol{\theta}_u,\\ &c(\boldsymbol{\theta}) \le 0,\end{aligned} \tag{33}$$

where $J_{\mathrm{o}}(\boldsymbol{\theta}), J_{\mathrm{r}}(\boldsymbol{\theta})$ are the two objective functions to be minimized, $\boldsymbol{\theta}_l, \boldsymbol{\theta}_u$ are the lower and upper bounds on the optimization variables, and $c(\boldsymbol{\theta})$ is a nonlinear constraint. The carrier frequency ω_c and desired tracking bandwidth ω_b are considered fixed inputs to the optimization procedure.

In order to evaluate the objectives, we use heuristics to obtain quantitative results for off-mode rejection and the step response. For each evaluation during the optimization procedure, the filter $T(s) = T_P(s;\boldsymbol{\theta})$ is generated and evaluated as follows. Here, the case $n = 3$ is considered in particular, however the presented material is trivially extended to any n.

1) OFF-MODE REJECTION, $J_{\mathrm{O}}(\boldsymbol{\theta})$

For the off-mode rejection, we evaluate the magnitude of $T(s)$ and $T_\perp(s)$ at N logarithmically spaced frequencies just outside the desired passband region. Specifically,

$$J_{\mathrm{o}}(\boldsymbol{\theta}) = \sqrt{\sum_{k=0}^{N-1}\left|T(j\omega_k^-)\right|^2 + \left|T^\perp(j\omega_k^+)\right|^2} \tag{34}$$

where the sampled frequencies ω_k^+, ω_k^- are given by

$$\omega_k^\pm = (\omega_c \pm \omega_b)\cdot 10^{\pm\frac{k}{N-1}}. \tag{35}$$

N should be large enough to ensure that the optimization procedure does not produce a highly localized minimization near a few samples, while low enough to ensure a sufficiently fast operation of the optimization procedure. We found $N = 50$ to give a good trade-off in terms of these considerations.

2) STEP RESPONSE RMS ERROR, $J_{\mathrm{R}}(\boldsymbol{\theta})$

The time-domain response of the demodulator is evaluated using a step response simulation of the demodulator, based on the root-mean-square (RMS) error of the estimated amplitude. This heuristic aims to fulfill the objective of a fast transient response with small estimation errors.

The evaluated demodulator is simulated for $T = 3\frac{2\pi}{\omega_b}$ seconds at a fixed sample time of $\Delta t = \frac{0.01}{f_c}$ seconds which gives $N = \frac{T}{\Delta t}$ discrete samples, in order to obtain the estimated amplitude a_k at increasing time steps k. This simulation time is sufficiently long for the dynamics to settle. The RMS error

heuristic is then given by

$$J_{\mathrm{r}}(\boldsymbol{\theta}) = \sqrt{\frac{1}{N}\sum_{k=0}^{N-1}(a^* - a_k)^2}, \tag{36}$$

with the reference amplitude fixed to $a^* = 1$.

3) OPTIMIZATION VARIABLES BOUNDS, $\boldsymbol{\theta}_l, \boldsymbol{\theta}_u$

The crossover frequencies ω_k are constrained such that the first two are located on each side of the carrier frequency ω_c, and the third one within the desired passband region, that is,

$$\begin{aligned} \omega_c \le \omega_1 \le \omega_c + 3\omega_b, \\ \max(\omega_c - 3\omega_b, \tfrac{1}{10}\omega_c) \le \omega_2 \le \omega_c, \\ \omega_c - \omega_b \le \omega_3 \le \omega_c + \omega_b. \end{aligned} \tag{37}$$

This placement of ω_k ensures that the filter takes the shape of a bandpass filter with its passband near ω_c. The factors are chosen to emphasize a wide range of permissible values to ensure versatility for the optimization procedure. The maximum function ensures that the constraints are valid for desired bandwidths ω_b up to the carrier frequency ω_c.

The constraints on ζ_k are likewise set to a wide range to emphasize maximum flexibility for the optimization procedure, where we allow them to range from 0.006 to 18 which permits both under- and overdamped dynamics.

4) TRACKING BANDWIDTH CONSTRAINT, $c(\boldsymbol{\theta})$

The nonlinear constraint c is used to constrain the resulting tracking bandwidth close to the desired bandwidth. We allow a 2 % shift away from the desired tracking bandwidth to increase the feasible solution space for effective operation of the optimization algorithm. That is,

$$c(\boldsymbol{\theta}) = |\omega_b - \omega_B| - 0.02\omega_b, \tag{38}$$

where ω_B is the amplitude tracking bandwidth of the considered demodulator, evaluated as described in Section II.

To obtain solutions for this problem, we use the Matlab function `gamultiobj` with default settings except for enabling parallelization. This function employs a multi-objective solver using a genetic algorithm [36].

Solutions of (33) are said to be *Pareto optimal* if any improvement in one objective cannot be achieved without a penalty in the other objective [36]. The set of Pareto optimal solutions is called the *Pareto front*. The Pareto front of the obtained solutions can be seen in Fig. 7. For the rest of this article, we pick two solutions for each of the low and high bandwidth settings, as marked in the figure. For each bandwidth setting, we choose one solution which is close to the `Lyap1` demodulator in terms of response time, and a second one which is closer to `Lyap3` in terms of response time. The two resulting demodulators are designated `MultiA` and `MultiB`, respectively.

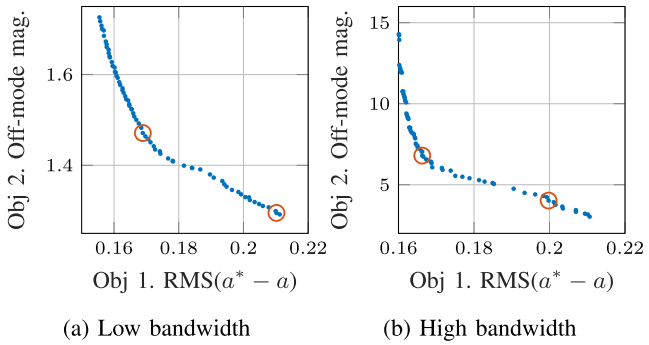

(a) Low bandwidth (b) High bandwidth

FIGURE 7. Pareto front of the multi-objective optimization solver. Dots (·) are individual solutions of the optimization problem, whereas circles (○) show the selected solutions.

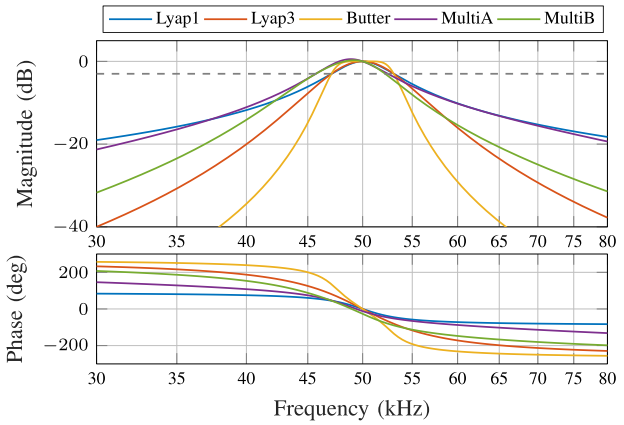

(a) Low bandwidth (3 kHz)

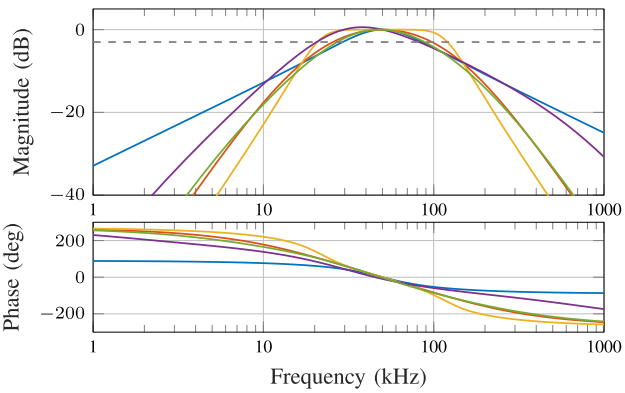

(b) High bandwidth (30 kHz)

FIGURE 8. Bode plot of the various bandpass filters $T(s)$ employed in the implemented generalized Lyapunov demodulator, with a carrier frequency specified at $f_c = 50$ kHz.

V. EXPERIMENTAL SETUP

A. DEMODULATORS

The experimental results are based on FPGA implementations of the generalized Lyapunov demodulator with a selection of the bandpass filters $T(s)$ presented in Section IV. In particular, the `Lyap3`, `Butter`, `MultiA` and `MultiB` relative order 3 filters, whose frequency responses are shown in Fig. 8.

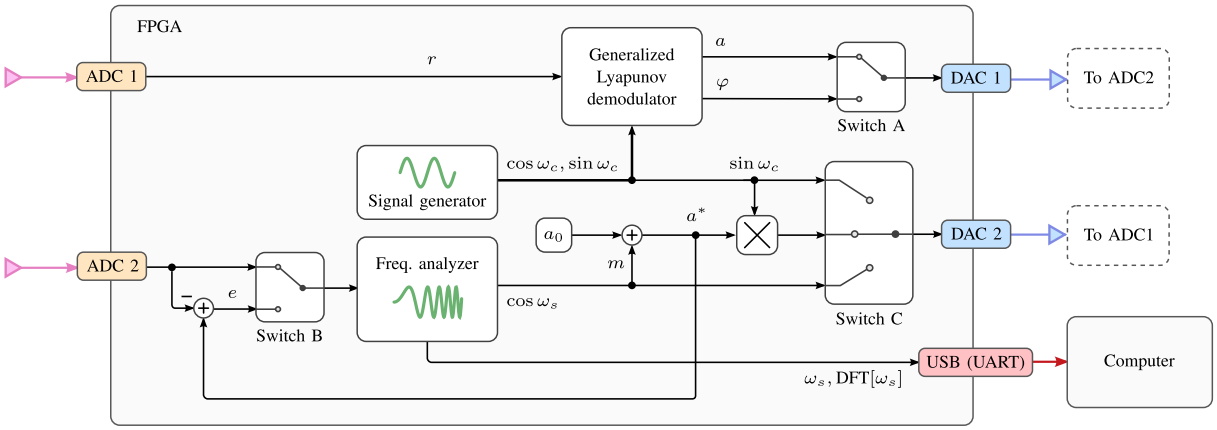

FIGURE 9. **Experimental setup. Different operating modes can be selected by the configuration of the switches. The shown configuration computes the amplitude tracking ($\mathcal{T}$) frequency response.**

Note that this figure shows the filter response ($r \to y$) as opposed to the off-mode rejection in Fig. 2(c). The generalized Lyapunov demodulators were implemented following Fig. 4, and use (12),(22), together with (7) to recover the estimated amplitude and phase. Since the performance characteristics of the demodulators can change drastically as their bandwidths approach the carrier frequency, all the demodulators were implemented at both a low bandwidth setting ($f_b = 3\,\text{kHz}$) and a high bandwidth setting ($f_b = 30\,\text{kHz}$), with the carrier frequency specified at $f_c = 50\,\text{kHz}$.

Additionally, the lock-in amplifier `LIA` and the standard Lyapunov demodulator `Lyap1` were implemented for comparison purposes. The implemented lock-in amplifier `LIA` uses a third-order Butterworth lowpass filter, identical to the one used in `Butter` before it is transformed to bandpass shape. This way, differences between `LIA` and `Butter` can therefore strictly be attributed to structural differences between the lock-in amplifier and generalized Lyapunov demodulator, as opposed to differences in filtering or tuning parameters.

B. HARDWARE

The demodulators were implemented on the Kintex-7 FPGA KC705 Evaluation Kit. For signal input and output, the FPGA was connected to an Abaco FMC151 ADC/DAC card featuring two 14-bit analog input channels with 250 MHz sampling frequency, and two 16-bit analog output channels at 800 MHz sampling frequency.

C. SOFTWARE

An overview of the experimental setup is illustrated in Fig. 9, which expands upon the setup in Fig. 1 with comparable symbols. The demodulators were partially written in Verilog and VHDL code, and partially in Matlab code and Simulink models which were subsequently converted to Verilog code using the HDL Coder toolbox [37]. The demodulators were implemented on the FPGA using a clock rate of 10 MHz, and use fixed-point arithmetic with the bit-width and scaling factors of signals determined using a combination of optimization procedures and manual tuning, along with simulations to ensure sufficient accuracy of the resulting numerical representations.

The sine/cosine reference carriers were generated using Xilinx DDS Compiler, and directed into a Simulink diagram implementing the generalized Lyapunov demodulator following Fig. 4. Each filter $T(s)$ was converted to a discrete transfer function with a sampling frequency of 10 MHz, using a least squares method to ensure a good match between the continuous and discrete model in the frequency domain. The filters were implemented in parallel, this way any of the demodulators can be selected at runtime by connecting the output from the desired filter. The rotation step is accomplished by the multiplication (22) using the rotation matrix (12), whereas the Cartesian to polar conversion represented by (7) is performed using a CORDIC algorithm [38]. CORDIC normally introduces a latency of one cycle per bit of accuracy [3]. However, in our implementation the selected FPGA clock rate was sufficiently low to perform the CORDIC algorithm in a single clock cycle.

D. FREQUENCY ANALYZER

There was also a desire to analyze and compare the performance of the demodulators at the high frequencies they are able to operate at. For this reason, a frequency analyzer was also designed and built into the FPGA, accompanying the demodulators. The demodulators and frequency analyzer were implemented in such a way that they can be used independently of each other, ensuring that results are obtained as if they were separate units. Their independence is ensured by making all communication between the demodulators and frequency analyzer go through the DAC and ADC channels, as seen in Fig. 9.

The frequency analyzer generates and outputs a sinusoidal sweep signal, and simultaneously computes the DFT using a second-order Goertzel algorithm at the current sweep frequency ω_s. Then each such frequency and DFT sample

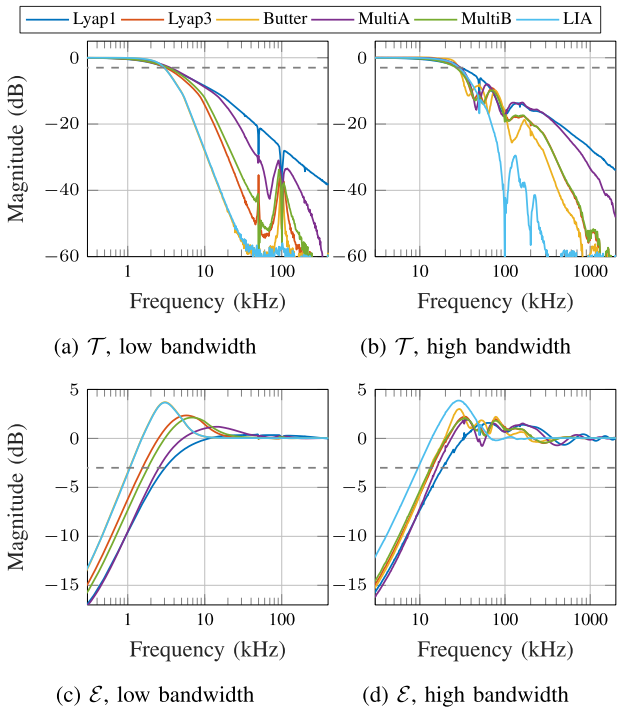

FIGURE 10. Amplitude tracking ($\mathcal{T}$) response and error ($\mathcal{E}$) response in the frequency domain, each of which are shown at the low (3 kHz) and high (30 kHz) bandwidth settings.

pair is transmitted to an external computer over a universal asynchronous receiver-transmitter (UART) connection. By performing the frequency domain conversion on the FPGA, the data bandwidth requirement is reduced from around 150 Mbit/s in the time domain to around 100 kbit/s in the frequency domain, which is manageable over the relatively low-bandwidth 115200 baud UART connection.

VI. RESULTS

A. FREQUENCY RESPONSE DATA

The demodulators were experimentally implemented on the FPGA at both the low and high bandwidth settings according to the setup in Section V. First, the amplitude tracking frequency response of the demodulators were recorded, which can be seen in Fig. 10. Then, off-mode rejection was measured by performing a frequency sweep on the carrier signal, while having the frequency analyzer configured to report the resulting amplitude estimate at steady-state. The results are shown in Fig. 11.

It can be observed that the `Lyap1` demodulator suffers from a substantially lower off-mode rejection, and its tracking response has a much softer roll-off compared to the rest. However, it has the greatest error bandwidth. This is mainly attributable to it being a relative order 1 filter whereas the others are relative order 3. In addition, note that at the low bandwidth setting the `Butter` and `LIA` demodulators are practically identical, however, at the large bandwidth setting

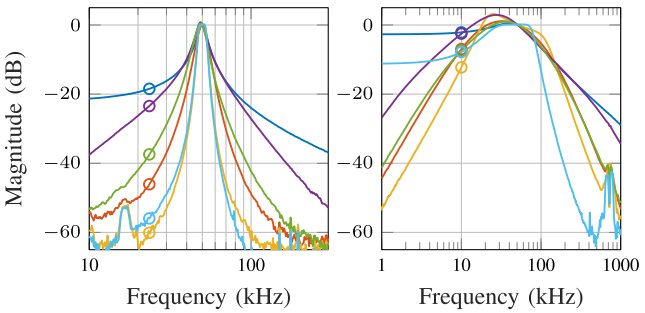

FIGURE 11. Off-mode rejection of the demodulators for a carrier frequency of $f_c = 50$ kHz. Color coded as in Fig. 10.

the `LIA` suffers from low error bandwidth and low off-mode rejection.

It can be seen that, particularly at the high bandwidth setting, the off-mode rejection of the `Lyap1` demodulator and `LIA` flattens out at lower frequencies, while the higher order Lyapunov demodulators approaches zero off-mode magnitude. This can be explained by considering a unit step input r. Then, for the `Lyap1` demodulator, the steady-state response of $T^{\perp}(s)$ corresponding to $T_1(s)$ is non-zero, which leads to a non-zero final value of the v_2 state. A non-zero v_2 further leads both the amplitude estimate and the off-mode magnitude to become non-zero as well. Conversely, for the higher order filters, $T^{\perp}(0) = 0$, so the off-mode magnitude approaches zero. In terms of the `LIA`, this can be attributed to its $2f_c$ mixing products, which leads to a non-zero amplitude estimate and thereby a non-zero off-mode magnitude at lower frequencies.

In Fig. 11(a) the LIA in particular shows an uncharacteristic pattern at high frequencies above 500 kHz. The source of this pattern is unclear to the authors, nevertheless, the pattern does not affect the conclusions drawn from these results.

B. STEP RESPONSE

The demodulator output on the FPGA was recorded in the time domain during a step of the reference amplitude a^* and phase φ^*, respectively. The results are shown in Fig. 12.

A clear inverse correlation between response times and off-mode rejection can be observed, with `Lyap1` and `MultiA` showing the fastest response but lowest off-mode rejection, whereas inversely for `Lyap3` and `Butter`. It can also be seen that at the low bandwidth setting, the `LIA` and `Butter` demodulators are again nearly identical due to their identical underlying filter. However, at the large bandwidth setting, the `LIA` reveals its detrimental $2f_c$ standing oscillations; instead, since `Butter` is a generalized Lyapunov demodulator, the error decays to zero in exponential time.

C. AFM TOPOGRAPHY IMAGING

The FPGA implementation of the demodulators was connected to a commercial AFM (Park Systems XE-70) for imaging experiments, according to the setup illustrated in

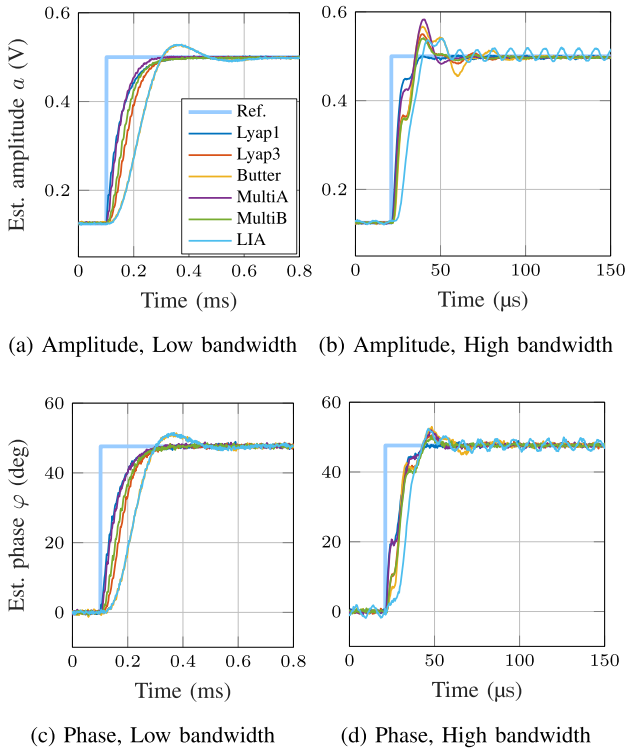

(a) Amplitude, Low bandwidth (b) Amplitude, High bandwidth

(c) Phase, Low bandwidth (d) Phase, High bandwidth

FIGURE 12. **Amplitude and phase estimation in the time domain.**

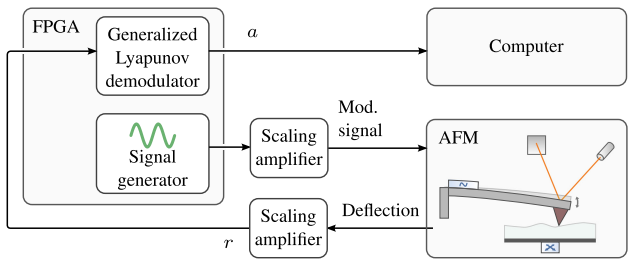

FIGURE 13. **AFM imaging setup with the generalized Lyapunov demodulator running on the FPGA for amplitude demodulation.**

Fig. 13. A high resonance frequency cantilever (PPP-NCHR) with a measured resonance frequency at 313.1 kHz was employed together with a height calibration sample (HS-100MG) with a stated height of 110 nm ± 3 %.

The first AFM experiment was setup to run a topography imaging experiment in intermittent contact mode, with a generalized Lyapunov demodulator being run at increasing bandwidths. This way, imaging limitations induced by a too low demodulation bandwidth are demonstrated. In order to render the demodulator the bottleneck in the AFM feedback loop, the AFM was operated in constant height mode, that is, with the vertical piezo actuator gain set very low. This way, the actuator maintains intermittent contact but does not track the topography. Instead, the topography appears entirely in the amplitude of the cantilever. The deflection amplitude voltage-to-height ratio was determined by exploiting the known step height of the sample.

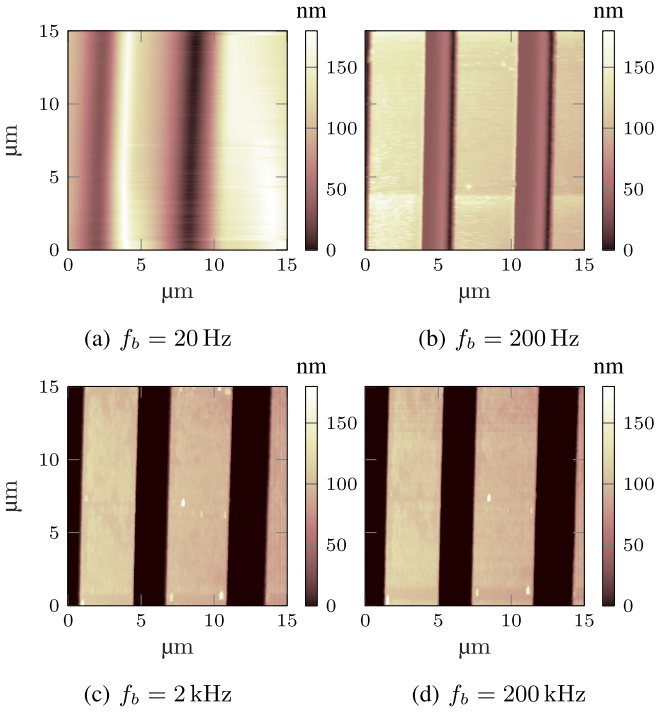

(a) $f_b = 20\,\text{Hz}$ (b) $f_b = 200\,\text{Hz}$

(c) $f_b = 2\,\text{kHz}$ (d) $f_b = 200\,\text{kHz}$

FIGURE 14. **AFM dynamic mode imaging experiment at constant height using the `Lyap3` demodulator at increasing demodulation bandwidths f_b.**

The calibration sample was scanned in an area with vertical step lines, using a scanning frequency of 5 Hz. The `Lyap3` demodulator was used at four bandwidth settings f_b, ranging from 20 Hz to 200 kHz, with a fixed carrier frequency $f_c = 313.1$ kHz. The resulting topography is shown in Fig. 14. It can be seen that there are major improvements to the sharpness of the topography steps with increasing demodulation bandwidth. The difference from 20 Hz to 2 kHz bandwidth is particularly noticeable, whereas the further increase to 200 kHz is close to imperceptible. These results demonstrate the need for sufficiently high bandwidths during AFM imaging.

D. AFM HIGHER HARMONIC IMAGING

The second AFM experiment intends to demonstrate the effect of increased off-mode rejection. The sample was imaged using an intermittent contact imaging procedure over the calibration sample, with the cantilever being driven close to the resonance frequency. Simultaneously, the 2nd-harmonic amplitude was recorded using two different demodulators, `Lyap1` and `Lyap3`, which were set up such that $f_c = 626.3$ kHz and their bandwidths tuned to $f_b = 10$ kHz.

The results are shown in Fig. 15. It can be seen that the standard deviation of the estimated amplitude of the `Lyap3` demodulator is significantly lower compared to the `Lyap1` demodulator, due to the increased off-mode rejection of the `Lyap3` demodulator.

The increased off-mode rejection of higher order demodulators will reduce the impact of noise, and notably also

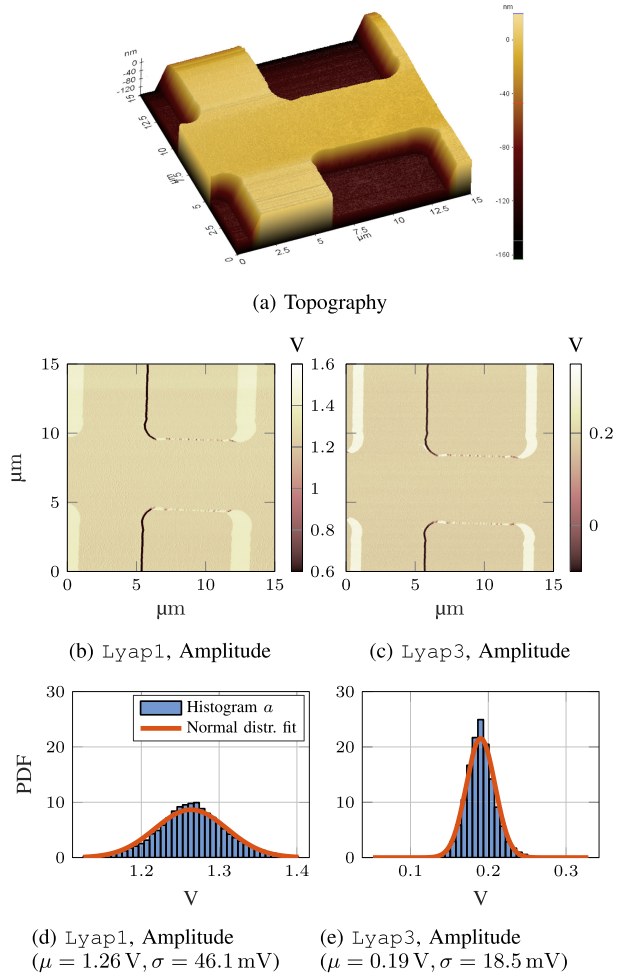

(a) Topography

(b) `Lyap1`, Amplitude

(c) `Lyap3`, Amplitude

(d) `Lyap1`, Amplitude ($\mu = 1.26\,\text{V}, \sigma = 46.1\,\text{mV}$)

(e) `Lyap3`, Amplitude ($\mu = 0.19\,\text{V}, \sigma = 18.5\,\text{mV}$)

FIGURE 15. AFM imaging experiment with 2nd harmonic amplitude estimates. (a) Sample topography. (b)-(c) Amplitude estimate a in terms of the voltage (V) output from the FPGA. (d)-(e) Probability density function (PDF) of the amplitude estimate over a flat section of the sample, and its normal distribution fit with the given mean μ and standard deviation σ.

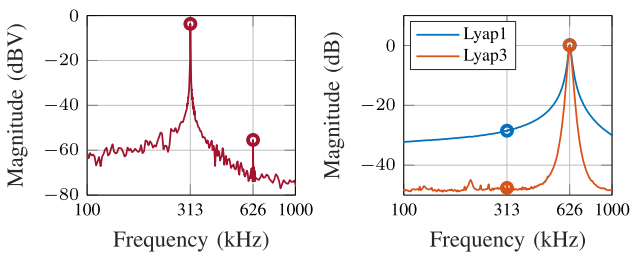

(a) (b)

FIGURE 16. (a) Cantilever deflection frequency response data while in-contact with the sample and with active AFM vertical feedback loop. (b) Off-mode rejection for demodulators tuned to the 2nd harmonic.

other harmonics present in the signal. To see the significance of off-mode rejection in this experiment, additional frequency domain experiments were conducted in this setup. The frequency response data of the cantilever deflection while in-contact with the sample was recorded and is shown in Fig. 16(a), where the magnitudes have been smoothed using a moving average filter and where the first and second harmonics are circled. Note that the first harmonic is 51.8 dB larger than the second harmonic, and that the demodulators were tuned to image the latter.

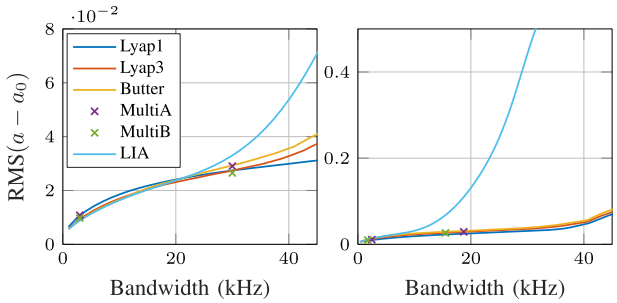

(a) Noise vs. tracking ($\mathcal{T}$) BW (b) Noise vs. error ($\mathcal{E}$) BW

FIGURE 17. Simulated noise response vs. demodulation bandwidth (BW).

Next, consider the off-mode rejection of both the `Lyap1` and `Lyap3` demodulators shown in Fig. 16(b). The `Lyap1` demodulator only has an attenuation of 28.5 dB at the first harmonic. The magnitude of the first harmonic compared to the second harmonic is significantly larger than the off-mode rejection, which results in the first harmonic contributing substantially to distorted output estimates. On the other hand, the off-mode rejection of the `Lyap3` demodulator is below the noise floor at 47.6 dB and properly rejects the contributions from the first harmonic. Thus, the distorted output of the `Lyap1` demodulator, due to its low off-mode rejection, explains the discrepancy between the mean amplitude levels and standard deviation shown in Fig. 15(d) and 15(e).

E. SIMULATED NOISE-BANDWIDTH RELATION

For each demodulator there is a trade-off between noise performance and demodulation bandwidth. The noise performance of a demodulator is numerically evaluated by applying band-limited white noise on top of a constant reference amplitude, and measuring the RMS of the resulting amplitude estimate error. These evaluations are performed numerically to enable noise measurement at a multitude of bandwidths within a reasonable time frame.

The noise performance is evaluated for all demodulators at increasing bandwidths and shown in Fig. 17. The `MultiA` and `MultiB` demodulators require manual selection of solutions at each bandwidth setting, thus, they are only shown at the bandwidths selected for experimental implementation. The results demonstrate the poor performance of the `LIA` at high bandwidths. The lock-in amplifier's $2f_c$ mixing products are not sufficiently attenuated at high bandwidths, resulting in detrimental noise performance. This is visible when evaluating the noise performance against the tracking bandwidth ($\mathcal{T}$), but is even more pronounced when evaluated against the error bandwidth ($\mathcal{E}$) due to the comparatively large magnitudes already displayed in its error frequency response.

TABLE 2 Summary of Demodulator Performance Metrics At the Low (top) and High (bottom) Bandwidth (BW) Settings.

	Tracking ($\mathcal{T}$) BW	Error ($\mathcal{E}$) BW	Off-mode rejection (higher is better)	Noise RMS (lower is better)	Relative order	Order
	kHz	kHz	dB			
`Lyap1`	3.2	3.1	18.5	10.1	1	2
`Lyap3`	3.1	1.5	46.1	12.5	3	6
`Butter`	3.0	1.1	60.1	14.2	3	6
`MultiA`	3.6	2.5	23.4	–	3	6
`MultiB`	3.4	1.8	37.4	–	3	6
`LIA`	3.0	1.1	56.0	14.3	3	3
`Lyap1`	30.2	18.5	2.1	29.1	1	2
`Lyap3`	28.4	13.9	7.0	33.8	3	6
`Butter`	28.6	13.2	12.3	36.4	3	6
`MultiA`	30.0	15.8	2.5	–	3	6
`MultiB`	26.6	13.4	7.4	–	3	6
`LIA`	29.0	9.6	7.8	419.1	3	3

Noise RMS values report simulated results at 3 kHz and 30 kHz error bandwidth, respectively.

F. DISCUSSION

The results are summarized in Table 2.

At the low bandwidth setting, the `Lyap1` demodulator stand out by its inability to effectively attenuate off-mode signals due to its relative order 1 characteristic. For the remaining demodulators, there is generally a trade-off between off-mode rejection and error bandwidth. In particular, the `Butter` generalized Lyapunov demodulator and the `LIA` demodulator are close to equivalent owing to both using the same underlying filter. On the other end, `MultiA` almost achieves error response magnitudes as low as `Lyap1` despite being a relative order 3 demodulator.

At the high bandwidth setting, there is an additional distinction between the standard and generalized Lyapunov demodulators `Lyap1`, `Lyap3`, `Butter`, `MultiA` and `MultiB`, and the lock-in amplifier `LIA`. Even though both `Butter` and `LIA` use the same underlying filter, the `LIA` performs much worse in terms of off-mode rejection, noise response, and error bandwidth due to its characteristic $2f_c$ standing oscillations which are not present in `Butter`. This distinction is an inherent property of the generalized Lyapunov demodulator structure, where there are no standing oscillations due to its exponential convergence properties. Furthermore, this is true regardless of the underlying filter employed.

In this sense, the generalized Lyapunov demodulator excel at both low and high bandwidth settings, thereby combining the strengths of the standard Lyapunov demodulator and the lock-in amplifier. Furthermore, the internal filter acts as an additional design degree of freedom that can be exploited to achieve the best trade-off between error bandwidth and off-mode rejection for any particular application.

VII. CONCLUSION

A generalized Lyapunov demodulator for amplitude and phase demodulation has been presented. It is based on an equivalent internal model representation of the standard Lyapunov demodulator, and then generalized to include higher order filtering capabilities; thereby making it highly suitable for applications where noise and off-mode harmonics need to be attenuated. Within the generalized Lyapunov demodulator there is additional design degree of freedom by shaping the bandpass pre-filter. The design of this filter has been discussed, and several filters have been proposed and implemented. The generalized Lyapunov demodulator has been experimentally implemented on an FPGA and compared to both the standard Lyapunov demodulator and the lock-in amplifier. The results demonstrate the ability of the generalized Lyapunov demodulator to combine the benefits from both of these state-of-the-art demodulators. *(a)* It has excellent off-mode rejection characteristics, comparable to the lock-in amplifier, and simultaneously *(b)* achieves high tracking bandwidths close to the carrier frequency without significant degradation, resembling the standard Lyapunov demodulator.

APPENDIX A
BANDWIDTH OF HIGHER ORDER LYAPUNOV FILTERS

In order to tune the bandwidth of the higher order Lyapunov demodulators, given by the filters $T_k(s)$, it is desirable to find the tuning parameters γ_k as a function of the tracking bandwidth ω_b.

First, consider the standard Lyapunov demodulator. The tracking bandwidth can be determined by the -3 dB passband bandwidth in $T(j\omega)$, as discussed in relation to Fig. 5. Recall

the first-order Lyapunov filter given by (27), that is

$$T_1(s) = \frac{\gamma s}{s^2 + \gamma s + \omega_c^2}. \tag{39}$$

It is seen that (39) is a second-order bandpass filter, thus, its -3 dB passband bandwidth is given by $\omega_{pb} = \gamma$. The approximate demodulator tracking bandwidth ω_b is half the passband bandwidth, as discussed in relation to the mixing products in (25), so that

$$\omega_b \triangleq \tfrac{1}{2}\omega_{pb} = \tfrac{1}{2}\gamma. \tag{40}$$

For the standard Lyapunov demodulator, (40) serves as a good tuning indicator for determining γ whenever a desired ω_b is specified, that is

$$\gamma = 2\omega_b. \tag{41}$$

Next, the higher order Lyapunov demodulators are considered. Let $T_k(s) \triangleq T_1(s)^k$. Then, solve $T_k(j\omega)$ for its solutions to the $1/\sqrt{2}$ magnitude,

$$\begin{aligned}
|T_k(j\omega)| &= \frac{1}{\sqrt{2}} \\
\left|\frac{\gamma_k j\omega}{-\omega^2 + \gamma_k j\omega + \omega_c^2}\right|^k &= \frac{1}{\sqrt{2}} \\
2^{\frac{1}{k}}\gamma_k^2\omega^2 &= (\omega_c^2 - \omega^2)^2 + \gamma_k^2\omega^2 \\
(2^{\frac{1}{k}} - 1)\gamma_k^2\omega^2 &= (\omega_c^2 - \omega^2)^2 \\
\sqrt{2^{\frac{1}{k}} - 1}\gamma_k\omega &= \pm(\omega_c^2 - \omega^2) \\
\omega^2 \pm b\omega - \omega_c^2 &= 0,
\end{aligned} \tag{42}$$

where we define $b \triangleq \sqrt{2^{\frac{1}{k}} - 1}\gamma_k$ and where it has been used that $\omega, \omega_c, \gamma_k > 0$. Solving (42) for ω gives the two positive solutions

$$\omega_{1,2} = \pm\frac{b}{2} + \frac{1}{2}\sqrt{b^2 + 4\omega_c^2}. \tag{43}$$

The passband bandwidth ω_{pb} can be expressed by the two solutions, such that

$$\omega_{pb} = \omega_1 - \omega_2 = b. \tag{44}$$

Then, using that the desired tracking bandwidth $\omega_b \triangleq \frac{1}{2}\omega_{pb}$ together with (44) and the definition of b, we can solve for γ_k as a function of ω_b. This gives the expression for the gain,

$$\gamma_k = \frac{2\omega_b}{\sqrt{2^{1/k} - 1}}. \tag{45}$$

REFERENCES

[1] S. S. Haykin, *Communication Systems*, 4th ed. New York, NY, USA: Wiley, 2001.

[2] R. G. Lyons, *Understanding Digital Signal Processing*, 3rd ed. Upper Saddle River, NJ, USA: Prentice Hall, 2010.

[3] D. Y. Abramovitch, "The demod squad: A tutorial on the utility and methodologies for using modulated signals in feedback loops," in *Proc. IEEE Conf. Control Technol. Appl.*, Montreal, QC, Canada, 2020, pp. 474–491.

[4] R. B. Northrop, *Introduction to Instrumentation and Measurements*. Bosa Roca, USA: CRC Press, 2014.

[5] D. Tse and P. Viswanath, *Fundamentals of Wireless Communication*, 1st ed. Cambridge, U.K.: Cambridge Univ. Press, 2005.

[6] R. Garcia and R. Perez, "Dynamic atomic force microscopy methods," *Surf. Sci. Rep.*, vol. 47, no. 6–8, pp. 197–301, 2002.

[7] D. Y. Abramovitch, S. B. Andersson, L. Y. Pao, and G. Schitter, "A tutorial on the mechanisms, dynamics, and control of atomic force microscopes," in *Proc. Amer. Control Conf.*, New York, NY, USA, 2007, pp. 3488–3502.

[8] M. G. Ruppert, D. M. Harcombe, M. R. P. Ragazzon, S. O. R. Moheimani, and A. J. Fleming, "A review of demodulation techniques for amplitude-modulation atomic force microscopy," *Beilstein J. Nanotechnol.*, vol. 8, no. 1, pp. 1407–1426, 2017.

[9] D. M. Harcombe, M. G. Ruppert, and A. J. Fleming, "A review of demodulation techniques for multifrequency atomic force microscopy," *Beilstein J. Nanotechnol.*, vol. 11, no. 1, pp. 76–91, 2020.

[10] K. S. Karvinen and S. O. R. Moheimani, "A high-bandwidth amplitude estimation technique for dynamic mode atomic force microscopy," *Rev. Sci. Instrum.*, vol. 85, no. 2, 2014, Art. no. 023707.

[11] D. Y. Abramovitch, "Low latency demodulation for atomic force microscopes, Part I efficient real-time integration," in *Proc. Amer. Control Conf.*, San Francisco, CA, USA, 2011, pp. 2252–2257.

[12] D. Y. Abramovitch, "Low latency demodulation for atomic force microscopes, Part II: Efficient calculation of magnitude and phase," *IFAC Proc. Volumes*, vol. 44, no. 1, pp. 12721–12726, 2011.

[13] M. G. Ruppert, K. S. Karvinen, S. L. Wiggins, and S. O. R. Moheimani, "A Kalman filter for amplitude estimation in high-speed dynamic mode atomic force microscopy," *IEEE Trans. Control Syst. Technol.*, vol. 24, no. 1, pp. 276–284, Jan. 2016.

[14] M. R. P. Ragazzon, M. G. Ruppert, D. M. Harcombe, A. J. Fleming, and J. T. Gravdahl, "Lyapunov estimator for high-speed demodulation in dynamic mode atomic force microscopy," *IEEE Trans. Control Syst. Technol.*, vol. 26, no. 2, pp. 765–772, Mar. 2018.

[15] D. M. Harcombe, M. G. Ruppert, M. R. P. Ragazzon, and A. J. Fleming, "Higher-harmonic AFM imaging with a high-bandwidth multifrequency Lyapunov filter," in *Proc. IEEE Int. Conf. Adv. Intell. Mechatronics*, Munich, Germany, 2017, pp. 725–730.

[16] D. M. Harcombe, M. G. Ruppert, M. R. P. Ragazzon, and A. J. Fleming, "Lyapunov estimation for high-speed demodulation in multifrequency atomic force microscopy," *Beilstein J. Nanotechnol.*, vol. 9, no. 1, pp. 490–498, 2018.

[17] M. G. Ruppert, D. M. Harcombe, S. I. Moore, and A. J. Fleming, "Direct design of closed-loop demodulators for amplitude modulation atomic force microscopy," in *Proc. Amer. Control Conf.*, Milwaukee, WI, USA, 2018, pp. 4336–4341.

[18] S. I. Moore, M. G. Ruppert, D. M. Harcombe, A. J. Fleming, and Y. K. Yong, "Design and analysis of low-distortion demodulators for modulated sensors," *IEEE/ASME Trans. Mechatronics*, vol. 24, no. 4, pp. 1861–1870, Aug. 2019.

[19] M. R. P. Ragazzon, S. Messineo, J. T. Gravdahl, D. M. Harcombe, and M. G. Ruppert, "Generalized Lyapunov demodulator for amplitude and phase estimation by the internal model principle," in *Proc. 8th IFAC Symp. Mechatronic Syst.*, Vienna, Austria, 2019, pp. 247–252.

[20] G. C. Goodwin, S. F. Graebe, and M. E. Salgado, *Control System Design*. Englewood Cliffs, NJ, USA: Prentice-Hall, 2000.

[21] B. A. Francis and W. M. Wonham, "The internal model principle of control theory," *Automatica*, vol. 12, no. 5, pp. 457–465, 1976.

[22] S. Messineo and A. Serrani, "Offshore crane control based on adaptive external models," *Automatica*, vol. 45, no. 11, pp. 2546–2556, 2009.

[23] V. Natarajan and J. Bentsman, "Robust rejection of sinusoids in stable nonlinearly perturbed unmodelled linear systems: Theory and application to servo," in *Proc. Amer. Control Conf.*, San Francisco, CA, USA, 2011, pp. 3289–3294.

[24] D. Lagrange, N. Mauran, L. Schwab, and B. Legrand, "Low latency demodulation for high-frequency atomic force microscopy probes," *IEEE Trans. Control Syst. Technol.*, vol. 29, no. 5, pp. 2264–2270, Sep. 2021.

[25] P. A. Ioannou and J. Sun, *Robust Adaptive Control*. Upper Saddle River, NJ, USA: Prentice-Hall, 1996.

[26] J. G. Proakis and D. G. Manolakis, *Digital Signal Processing: Principles, Algorithms, and Applications*, 3rd ed. Upper Saddle River, NJ, USA: Prentice-Hall, 1996.
[27] S. Skogestad and I. Postlethwaite, *Multivariable Feedback Control: Analysis and Design*, 2nd ed. Chichester, England: Wiley, 2007.
[28] J. C. Doyle, B. A. Francis, and A. Tannenbaum, *Feedback Control Theory*. New York, NY, USA: Macmillan, 1992.
[29] M. W. Spong, S. Hutchinson, and M. Vidyasagar, *Robot Model. and Control*. Chichester, U.K.: Wiley, 2005.
[30] R. Garcia and E. T. Herruzo, "The emergence of multifrequency force microscopy," *Nature Nanotechnol.*, vol. 7, no. 4, pp. 217–226, 2012.
[31] M. G. Ruppert, D. M. Harcombe, and S. O. R. Moheimani, "High-bandwidth demodulation in MF-AFM: A Kalman filtering approach," *IEEE/ASME Trans. Mechatronics*, vol. 21, no. 6, pp. 2705–2715, Dec. 2016.
[32] A. Antoniou, *Digital Signal Processing: Signals, Systems and Filters*, 1st ed. New York, NY, USA: McGraw-Hill, 2005.
[33] H. A. Nguyen, Z. van Iperen, S. Raghunath, D. Abramson, T. Kipouros, and S. Somasekharan, "Multi-objective optimisation in scientific workflow," *Procedia Comput. Sci.*, vol. 108, pp. 1443–1452, 2017.
[34] M. Pearce, B. Mutlu, J. Shah, and R. Radwin, "Optimizing makespan and ergonomics in integrating collaborative robots into manufacturing processes," *IEEE Trans. Automat. Sci. Eng.*, vol. 15, no. 4, pp. 1772–1784, Oct. 2018.
[35] E. Kelasidi, M. Jesmani, K. Y. Pettersen, and J. T. Gravdahl, "Locomotion efficiency optimization of biologically inspired snake robots," *Appl. Sci.*, vol. 8, no. 1, 2018, Art. no. 80.
[36] K. Deb, *Multi-Objective Optimization Using Evolutionary Algorithms*. Chichester, U.K.: Wiley, 2001.
[37] The MathWorks, Inc., "HDL coder toolbox," Natick, Massachusetts, USA, Accessed on: Dec. 13, 2021. [Online]. Available: https://www.mathworks.com/help/hdlcoder/
[38] J. E. Volder, "The CORDIC trigonometric computing technique," *IRE Trans. Electron. Comput.*, vol. EC-8, no. 3, pp. 330–334, 1959.

MICHAEL R. P. RAGAZZON received the M.Sc. and Ph.D. degrees in engineering cybernetics from the Norwegian University of Science and Technology (NTNU), Trondheim, Norway, in 2013 and 2018, respectively. He pursued his interests in atomic force microscopy as a Postdoctoral Researcher with NTNU until 2021. His main research interests include control theory and parameter estimation, and their application to extending the imaging capabilities of dynamic mode, and multifrequency atomic force microscopy.

SAVERIO MESSINEO (Member, IEEE) received the Ph.D. degree in control systems from the Norwegian University of Science and Technology, Trondheim, Norway, in 2009. During his Ph.D. studies, he spent more than two years, from 2006 to 2008, as a Visiting Ph.D. Student with the Department of Electrical and Computer Engineering, The Ohio State University, Columbus, OH, USA, under the scientific supervision of Prof. Andrea Serrani. During his research career, he has been engaged in the investigation of problems within the area of control systems, either within an industrial framework (e.g., as a Research Scientist with the Schlumberger Gould Research Centre, Cambridge, U.K.), or in academia, while holding the post of an Associate Professor in control systems with NTNU. From a theoretical standpoint, his research interests include adaptive and robust nonlinear control design, nonlinear observer design, quasi-periodic disturbance rejection and nonlinear output regulation. In relation to the applicative side, he has been working in the experimental investigation of areas, such as offshore crane control for marine operations, control of directional drilling systems for petroleum engineering applications, control of atomic force microscopes, and active vibration rejection for metrology platforms within the context of precision control for mechatronics systems. He is currently a Senior Scientist within the Embedded AI Department, Silicon Austria Labs, Linz, Austria.

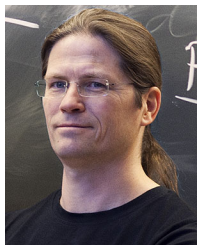

JAN TOMMY GRAVDAHL (Senior Member, IEEE) received the Siv.ing and Dr.ing degrees in engineering cybernetics from the Norwegian University of Science and Technology (NTNU), Trondheim, Norway, in 1994 and 1998, respectively. Since 2005, he has been a Professor with the Department of Engineering Cybernetics, NTNU, where he was also the Head of Department during 2008–2009. He has supervised the graduation of 160 M.Sc. and 15 Ph.D. candidates. He has authored or coauthored five books and more than 250 papers in international conferences and journals. His current research interests include mathematical modeling and nonlinear control in general, in particular applied to turbomachinery, marine vehicles, spacecraft, robots, and high-precision mechatronic systems. Since 2020, he has been an Associate Editor for IEEE TRANSACTIONS ON CONTROL SYSTEMS TECHNOLOGY. He was the Senior Editor of the IFAC journal *Mechatronics* during 2016–2020, and an Associate Editor for the journal *Simulation Modelling Practice and Theory* during 2007–2011. He has been on the Editorial Board and IPC for numerous international conferences. In 2000 and 2017, he was awarded the IEEE Transactions on Control Systems Technology Outstanding Paper.

DAVID M. HARCOMBE received the Bachelor of Engineering degree in electrical engineering with the University Medal and the Ph.D. degree in electrical engineering from The University of Newcastle, Callaghan, NSW, Australia, in 2016 and 2020, respectively. His research interests include multifrequency atomic force microscopy, microelectromechanical systems, high-speed demodulation, and inertially stabilized platforms for optical systems.

MICHAEL G. RUPPERT (Member, IEEE) received the Dipl.-Ing. degree in automation technology from the University of Stuttgart, Stuttgart, Germany, in 2013, and the Ph.D. degree in electrical engineering from The University of Newcastle, Callaghan, NSW, Australia, in 2017. From 2015 to 2016, he was a Visiting Researcher with The University of Texas at Dallas, Richardson, TX, USA. He is currently a Research Fellow with The University of Newcastle. His research interests include the development of estimation, control, and self-sensing approaches for microelectromechanical systems, such as piezoelectric microcantilevers and nanopositioning systems for multifrequency and single-chip atomic force microscopy.

Dr. Ruppert's research has been recognized with the election to 2021 Fresh Scientist for NSW, Best Conference Paper Award at the 2019 International Conference on Manipulation, Automation and Robotics at Small Scales, 2018 IEEE TRANSACTIONS ON CONTROL SYSTEMS TECHNOLOGY Outstanding Paper Award, and the 2017 University of Newcastle Higher Degree by Research Excellence Award.